# Surface electric fields for North America during historical geomagnetic storms

Lisa H. Wei,[1] Nicole Homeier,[1] and Jennifer L. Gannon[2]

[1]    To better understand the impact of geomagnetic disturbances on the electric grid, we recreate surface electric fields from two historical geomagnetic storms—the 1989 "Quebec" storm and the 2003 "Halloween" storms. Using the Spherical Elementary Current Systems method, we interpolate sparsely distributed magnetometer data across North America. We find good agreement between the measured and interpolated data, with larger RMS deviations at higher latitudes corresponding to larger magnetic field variations. The interpolated magnetic field data are combined with surface impedances for 25 unique physiographic regions from the United States Geological Survey and literature to estimate the horizontal, orthogonal surface electric fields in 1 min time steps. The induced horizontal electric field strongly depends on the local surface impedance, resulting in surprisingly strong electric field amplitudes along the Atlantic and Gulf Coast. The relative peak electric field amplitude of each physiographic region, normalized to the value in the Interior Plains region, varies by a factor of 2 for different input magnetic field time series. The order of peak electric field amplitudes (largest to smallest), however, does not depend much on the input. These results suggest that regions at lower magnetic latitudes with high ground resistivities are also at risk from the effect of geomagnetically induced currents. The historical electric field time series are useful for estimating the flow of the induced currents through long transmission lines to study power flow and grid stability during geomagnetic disturbances.

Citation: Wei, L. H., N. Homeier, and J. L. Gannon (2013), Surface electric fields for North America during historical geomagnetic storms, *Space Weather*, *11*, 451–462, doi:10.1002/swe.20073.

## 1.  Introduction

[2]   Geomagnetic disturbances, or GMDs, are the result of the interaction between solar plasma and the geomagnetic field when a coronal mass ejection reaches the Earth. GMDs often result in large magnetic and electric field fluctuations on the ground, which can induce geomagnetically induced currents (GICs) with high amplitudes in power lines, pipelines, railway systems, and telecommunication cables [*Boteler et al.*, 1998]. GIC flowing through the electric grid can be extremely disruptive—damaging transformers [*Kappenman and Albertson*, 1990; *Molinski*, 2002] and creating unstable grid operation conditions [e.g., *Forbes and St. Cyr*, 2012] that lead to generator/capacitor tripping and/or voltage collapse [*Albertson et al.*, 1981;

*Schlueter*, 1998] and resulting in widespread power outages [*Kappenman*, 2004]. Transformer damage and power outages are of even greater concern these days, with the increasing reliance on electricity for everyday life and an aging grid infrastructure more vulnerable to damage.

[3]   Understanding the risk of power outages posed by GMDs requires detailed modeling of GIC flow through the electric grid. GIC flow can be estimated by integrating the electric field along transmission lines and solving for the network of direct currents [e.g., *Pirjola*, 2008; *Horton et al.*, 2012]. Thus, realistic scenarios of surface electric field fluctuations are essential to study GIC flow during GMDs. Much progress has been made in the study of GICs in the last few decades, with particular focus in regions of high latitude most strongly affected by GMDs [e.g., *Kappenman et al.*, 2000; *Boteler*, 2001; *Erinmez et al.*, 2002; *Pirjola*, 2008; *Wik et al.*, 2008; *Pulkkinen et al.*, 2012; *Viljanen et al.*, 2012].

[4]   Methods have been developed to interpolate sparsely distributed magnetic field measurements across large regions using the method of Spherical Elementary Current Systems [*Amm*, 1997; *Amm and Viljanen*, 1999]. The surface magnetic fields can be combined with local surface impedance models using the plane wave method to estimate the local electric field [e.g.,

---

[1]Atmospheric and Environmental Research, Inc., Lexington, Massachusetts, USA.
[2]Geomagnetism Program, U.S. Geological Survey, Golden, Colorado, USA.

Corresponding author: L. H. Wei, Atmospheric and Environmental Research, Inc., 131 Hartwell Avenue, Lexington, MA, USA. (lwei@aer.com)

**Table 1.** Magnetometer Stations and Storm Time Ranges Included in Our Electric Field Calculations

| Storm | Stations | Time Range (UT) |
|---|---|---|
| 1989 "Quebec" | BSL, DLR, FCC, FRD, FRN, GLN, MEA, NEW, OTT, PBQ, STJ, TUC, VIC | 12 Mar 89 00:00:00–15 Mar 89 12:00:00 |
| 2003 "Halloween" | BOU, BSL, DLR, FCC, FRD, FRN, MEA, OTT, PBQ, SJG, STJ, TUC, VIC | 29 Oct 03 00:00:00–01 Nov 03 00:00:00 |

*Radasky et al.*, 1993; *Viljanen et al.*, 2004; *Kappenman and Radasky*, 2005]. In the United Kingdom, modeling of GIC flow through the high voltage network have been validated, with a real-time computational system in place since 2000 [*Kappenman et al.*, 2000; *Erinmez et al.*, 2002; *Thomson et al.*, 2005]. The Finnish Meteorological Institute have also developed a GIC nowcasting service [*Viljanen et al.*, 2006] that derives GIC levels from real-time magnetic field measurements.

[5] In the United States, there have been efforts to model surface electric fields and GICs on a regional basis, with emphasis in Minnesota, since the early 1980s [e.g., *Kappenman et al.*, 1981, 2000]. More recently, Metatech led the first US-wide modeling of GIC in high-voltage transmission lines [see *Kappenman and Radasky*, 2005; *Kappenman*, 2010]. Aside from these efforts, there exists few studies of the large-scale effects of GMDs in the United States, perhaps due to the difficulty in obtaining complete grid information from the large number of companies operating the grid in various regions.

[6] In this paper, we consider the large-scale impact of GMDs in the United States and Canada by creating time series of surface electric field maps of the 1989 "Quebec" and 2003 "Halloween" geomagnetic disturbances using a new set of 1-D regional resistivity models created by the United States Geological Survey [*Fernberg*, 2012]. Section 2 describes the input historical magnetic field measurements and earth resistivity models used in this study. Section 3 compares the measured magnetic field time derivatives against interpolated values to evaluate the method of Spherical Elementary Current Systems. In section 4, we show the resulting surface electric field maps from parts of the two storms and compare the response of different surface impedance models to the same magnetic field input. We discuss our results and possible applications for the storm scenarios in section 5 and summarize major results in section 6.

## 2. Data

[7] Archival magnetometer data for historical storms are available for dates as far back as the early 1980s. For this study, we choose the two storms in this time range that had the most impact on power systems. The 1989 "Quebec" storm was famously known for inducing harmonics that tripped protective systems on several static VAR (reactive volt-ampere) compensators, collapsing the Hydro-Quebec power grid. More than six million people lost power for 9 h at an economic cost estimated

to be around 13.2 billion Canadian dollars [*Bolduc*, 2002]. The 2003 "Halloween" storms occurred over the span 3 days. During this period, parts of Malmö in Sweden experienced a blackout attributed to the combination of harmonic distortions caused by geomagnetically induced currents and incorrectly set protective relay thresholds [*Pulkkinen et al.*, 2005]. Additionally, 12 transformers in South Africa suffered significant damage, necessitating their removal from service [*Gaunt and Coetzee*, 2007].

### 2.1. Magnetic Field Data

[8] For the 2003 "Halloween" storm, we utilize the "Definitive" magnetic field data product with an 1 min sampling rate compiled by the International Real-Time Magnetic Observatory Network (Intermagnet, http://www.intermagnet.org/). The Definitive data have been corrected for baseline variations, with spikes removed and gaps filled. We convert the horizontal ($H$) and declination ($D$) data from Intermagnet for U.S. magnetometer stations into northward ($X$) and eastward ($Y$) data following $X = H \cos D$, $Y = H \sin D$. Data from Canadian magnetometer stations are provided in the $X$ and $Y$ format. At each station, we subtract from the data the mean magnetic field for that period for each direction.

[9] Because Intermagnet does not have data prior to 1991, we obtain the "Final" magnetic field data product from SuperMAG (http://supermag.uib.no) for the 1989 "Quebec" storm, also sampled in 1 min time steps. SuperMAG removes the baseline in three steps: a daily baseline, a yearly baseline, and whatever residual offsets that remain [*Gjerloev*, 2012]. For both data sets, magnetometer stations missing data for more than 120 consecutive time steps (2 h) are excluded. Data missing less than 120 consecutive time steps are linearly interpolated—we discuss uncertainties in the electric field estimate due to the interpolation in section 4.4. We list date ranges and available North American magnetometer stations for both storms in Table 1 and show the station locations in Figure 1.

[10] We note that the Intermagnet Definitive data and SuperMAG Final data are different products derived from the same set of magnetometer observatory data with different baselining methods. Section 4.4 compares electric fields derived from the two different compilations.

### 2.2. Regional Resistivity Models

[11] The plane wave method (see section 4.1) relates horizontal electric field variations to magnetic field variations by the ground surface impedance ($Z$), which
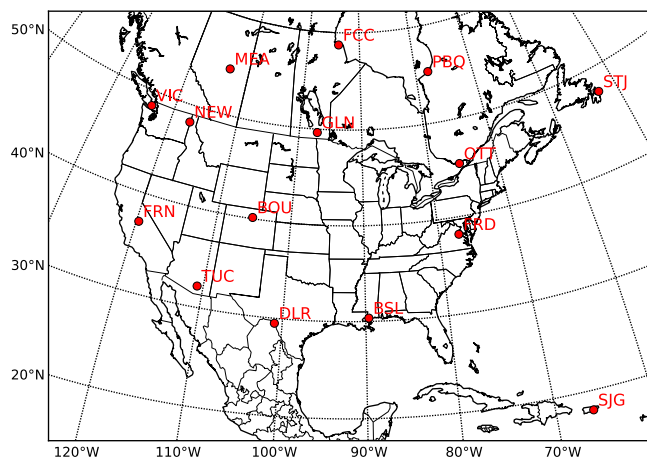
**Figure 1.** Locations of magnetometer stations with magnetic field data during the 1989 and/or 2003 geomagnetic storms. With the exception of FCC, SJG, and STJ, all stations are within the grid of interpolated magnetic fields.

depends on the resistivity of regional Earth layer properties and changes with geological composition. There exist many localized measurements and models of ground resistivity, produced for individual scientific analyses. For uniformity, we utilize the U.S.-wide resistivity map compiled by the United States Geological Survey (USGS), which provides 20 unique 1-D layered Earth resistivity models for 31 contiguous physiographic regions across the continental United States [*Fernberg*, 2012]. Note that the highly resistive central core of the Adirondack Mountains is distinguished from the rest of the region by a box roughly following Figure 3 of *Carr et al.* [2000].

[12] While these physiographic regions are broadly defined and do not reflect local nonuniformities on the scale of approximately hundred kilometers, they represent a reasonable first-order representation of the U.S. resistivity distribution and the most complete data set to date for the U.S., and is sufficient for large-scale studies of surface electric fields.

[13] We supplement the USGS data with five realistic layered Earth resistivity models for Canada described in *Pirjola et al.* [2009]: the "Quebec," "Ontario—Model 1," "Southern Manitoba," "British Columbia," and "Nova Scotia" (QUE, ONT, MAN, BRC, and NOV, respectively). We also extend the Great Plains and Central Lowland physiographic regions northward for the Alberta, Saskatchewan, and southwestern Manitoba provinces in Canada. Dark lines in Figure 2 demarcate the different physiographic regions used in this study. Surface impedances for the supplemental regions are estimated from the layered Earth models following equation (A2) from *Pulkkinen et al.* [2012] for the same frequency range ($10^{-5}$–0.1 Hz) as the USGS models.

## 3. Magnetic Field Interpolation

### 3.1. The Spherical Elementary Current System (SECS) Method

[14] Because magnetometer stations are often sparse in number and separated by large distances (Figure 1), we utilize the method of Spherical Elementary Current System (SECS) [*Amm*, 1997; *Amm and Viljanen*, 1999; *Pulkkinen et al.*, 2003] to interpolate the magnetic field at a given location from existing measurements. The SECS method assumes that the ground magnetic field can be represented by a system of divergence-free equivalent currents in the ionosphere. By solving for the scaling factors of the ionospheric current systems with the magnetometer measurements, we can then estimate the ground magnetic field at any location using a linear combination of the equivalent current systems.

[15] The SECS method has been shown to accurately reproduce measured magnetic fields in Canadian and European magnetic observatory networks [*McLay and Beggan*, 2010]. Data from 13 magnetometer stations are used for each of the storms (Table 1).

[16] For this method, we define a grid of 209 divergence-free equivalent elementary current systems 5° apart in the ionosphere, 100 km above the ground. The current systems are related to the observations by:

$$\mathbf{T} \cdot \mathbf{I} = \mathbf{Z}, \qquad (1)$$

where $\mathbf{T}$ is a matrix containing the $\theta$ or $\phi$ component of the ground magnetic field effect by the elementary current system [*Amm and Viljanen*, 1999, equations (9) and (10)] with a scaling factor of 1 A, $\mathbf{I}$ is a vector of scaling factors for the current systems, and $\mathbf{Z}$ is a vector with the magnetic field observations. Because the number of magnetic
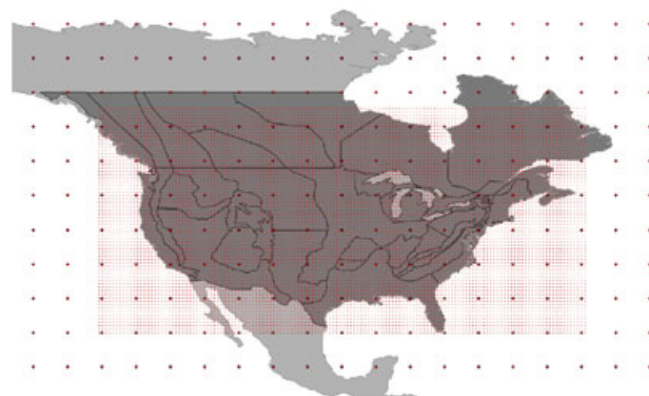


**Figure 2.** Physiographic regions for the United States and southern Canada (dark lines), from the USGS and *Pirjola et al.* [2009], respectively. Large-filled circles represent the grid of equivalent elementary current systems in the ionosphere spaced 5° apart used to interpolate magnetic field data. Small red dots show the grid of 9100 locations spaced 0.5° apart where the magnetic field data is interpolated.

**Table 2.** Comparison Between Measured and Interpolated Magnetic Field Time Derivatives at Magnetometer Stations[a]

| Station | Max $|dB/dt_{obs}|$ North (nT/s) | Max $|dB/dt_{obs}|$ East (nT/s) | RMSD North (nT/s) | RMSD East (nT/s) | RMSD/Max $|dB/dt_{obs}|$ North | RMSD/Max $|dB/dt_{obs}|$ East |
|---|---|---|---|---|---|---|
| 1989 "Quebec" | | | | | | |
| BSL | 4.5 | 7.7 | 0.87 | 0.95 | 0.19 | 0.12 |
| DLR | 0.8 | 1.8 | 0.30 | 0.51 | 0.38 | 0.29 |
| FRD | 3.5 | 4.0 | 0.99 | 0.83 | 0.28 | 0.21 |
| FRN | 1.8 | 1.4 | 0.78 | 0.72 | 0.43 | 0.53 |
| GLN | 5.2 | 4.9 | 1.40 | 0.92 | 0.27 | 0.19 |
| MEA | 8.4 | 13.6 | 2.22 | 1.60 | 0.27 | 0.12 |
| NEW | 4.4 | 5.6 | 1.34 | 1.03 | 0.31 | 0.18 |
| OTT | 4.7 | 7.8 | 1.81 | 1.13 | 0.38 | 0.15 |
| PBQ | 3.7 | 5.5 | 1.30 | 1.28 | 0.35 | 0.23 |
| TUC | 1.5 | 1.9 | 0.43 | 0.47 | 0.29 | 0.25 |
| VIC | 3.9 | 9.6 | 1.39 | 1.00 | 0.36 | 0.10 |
| 2003 "Halloween" | | | | | | |
| BOU | 2.1 | 1.5 | 0.39 | 0.29 | 0.19 | 0.20 |
| BSL | 0.9 | 1.7 | 0.30 | 0.49 | 0.33 | 0.29 |
| DLR | 1.0 | 1.9 | 0.10 | 0.38 | 0.10 | 0.20 |
| FRD | 1.5 | 2.9 | 0.79 | 0.49 | 0.51 | 0.17 |
| FRN | 1.5 | 1.8 | 0.27 | 0.18 | 0.18 | 0.10 |
| MEA | 5.7 | 11.0 | 2.52 | 1.20 | 0.44 | 0.11 |
| OTT | 4.9 | 12.5 | 1.42 | 1.14 | 0.29 | 0.09 |
| PBQ | 6.5 | 11.5 | 2.14 | 1.53 | 0.33 | 0.13 |
| TUC | 1.2 | 1.8 | 0.22 | 0.14 | 0.19 | 0.08 |
| VIC | 2.2 | 3.0 | 0.71 | 0.48 | 0.32 | 0.16 |

[a]Only stations within the interpolation grid are included. North and east $|dB/dt_{obs}|$ values are from SuperMAG for the 1989 "Quebec" storm and Intermagnet for the 2003 "Halloween" storms. The root-mean-square deviation (RMSD) is calculated for 20 min intervals around the 10 largest values of $|dB/dt_{obs}|$ for each station during each storm following equation (2), and averaged for each direction. Similarities in ratio of RMSD to max $|dB/dt_{obs}|$ between most stations suggest that the larger scatter observed in the northern stations (GLN, MEA, NEW, OTT, PBQ, and VIC) reflect larger magnetic field fluctuations at those locations. Note that the magnetic field data are separated by 1 min intervals but divided by 60 s to determine $dB/dt$.

field observations are typically much less than the number of ionospheric currents, we solve for **I** using singular value decomposition (SVD) [*Press et al.*, 2007] to invert the **T** matrix. For each time step over the duration of the storm, we solve for the vector of scaling factors.

[17] After obtaining the scaling factors for the equivalent current systems, we calculate the magnetic fields at 9100 grid locations spaced 0.5° apart across North America by constructing a second **T** matrix that relates the interpolation grid to the current systems. The dot product between the second **T** matrix and the vector of scaling factors **I** provides an estimate of the magnetic field at each of the 9100 locations. Figure 2 shows the extent of both the elementary current grid and the interpolation grid.

[18] We note that *Pulkkinen et al.* [2003] extends the SECS method by considering two layers of equivalent currents—an external layer in the ionosphere and an internal layer below the surface of the Earth. Because we are only interested in horizontal magnetic fields on the surface of the Earth and not the vertical component, we do not need to include the internal current layer in our interpolation.

### 3.2. Validation

[19] To validate the SECS interpolation method, we perform the interpolation multiple times for each storm—each time excluding data from a magnetometer station within the grid of 9100 points. Because electric field amplitudes are directly related to the time variations of the magnetic field, we compare the time derivative of the interpolated magnetic field (dB/dt) at the location closest to the station to the time derivative of the measured magnetic field. Stations not in the interpolation grid (FCC, SJG, and STJ) and time ranges missing data are excluded from the comparison.

[20] To compare the observed and interpolated data, we calculate the root-mean-square deviation (RMSD) for 20 min intervals around each of the 10 largest values of $|dB/dt_{obs}|$ for each station during each storm:

$$RMSD = \sqrt{\sum (dB/dt_{obs} - dB/dt_{int})^2 / N}, \qquad (2)$$

where $N$ is the number of time steps (21) in the interval, $dB/dt_{obs}$ is the observed magnetic field time derivative, and $dB/dt_{int}$ is the time derivative of the SECS interpolated magnetic field discussed in section 3.1. We average the 10 values of RMSDs for each station during each storm and list the results of the comparison, separated by magnetic field orientation (north, east), in Table 2.

[21] Figures 3 and 4 show the comparison between measured and interpolated surface magnetic field time derivatives for the stations with the lowest and highest values of RMSD, during the most active 4 h at that location for the 1989 and 2003 storms, respectively. For the low RMSD locations (e.g., DLR and TUC), the amplitude variations of the interpolated magnetic field time derivatives appear to be well-matched at most time steps, though a few large spikes were missed during the 1989
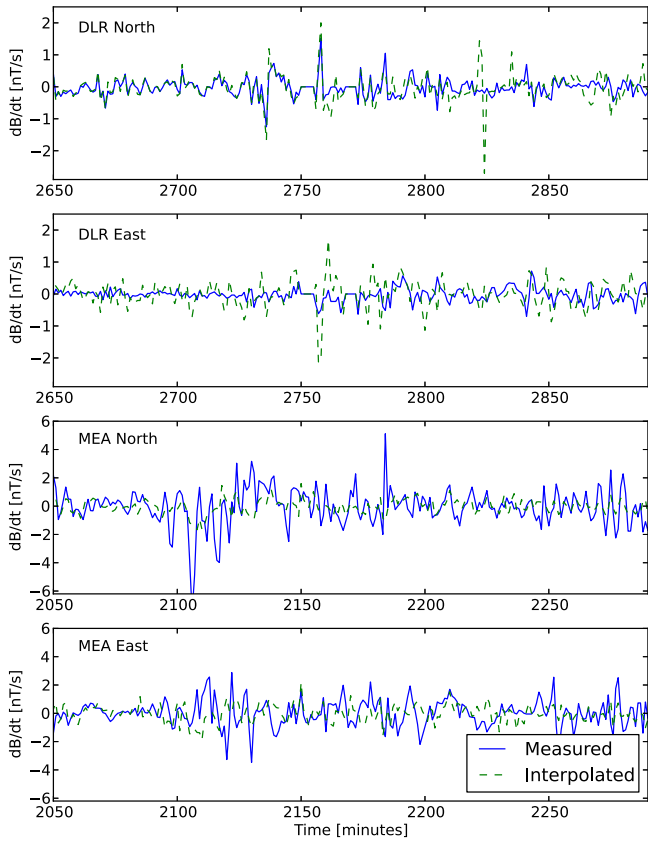
**Figure 3.** Comparison of the measured (solid blue lines) and interpolated (dashed green lines) magnetic field time derivatives for the 1989 "Quebec" storm for the station with the lowest (DLR) and highest (MEA) average RMS deviation. Missing magnetic field data are set to zero and not included in the RMSD calculation. Note that the magnetic field data are separated by 1 min intervals but divided by 60 s to determine $dB/dt$.

storm. The RMS deviations are larger for stations at higher latitudes in Canada (i.e., GLN, MEA, NEW, OTT, PBQ, and VIC).

[22] These larger RMS deviations appear to reflect larger magnetic field fluctuations at higher latitudes. When we consider the RMSD normalized to the maximum observed magnetic field time derivative in that direction ($|dB/dt_{obs}|$), there are no large differences between magnetometer stations at low and high latitudes. The normalized values are also quite similar between the two storms (RMSD/max$|dB/dt_{obs}|$ = 0.27 and 0.22, averaged over comparison stations, for the 1989 and 2003 storms, in the range of ~0.1–0.5).

[23] Overall, the SECS method does a good job interpolating the sparsely distributed magnetometer field measurements in many places, extending data from 13 magnetometer locations to 9100 points across the United States and Canada. The accuracy of the SECS method appears to decrease at locations with larger magnetic

field fluctuations, which tends to affect regions at higher latitudes.

## 4. Electric Field Variations During a Geomagnetic Storm

[24] Given the interpolated magnetic fields (section 3) and surface impedance models (section 2.2) across much of North America, we can then estimate the surface electric fields during the two historic geomagnetic storms.

### 4.1. Plane Wave Method

[25] We estimate the surface electric field during storms using the plane wave method [*Cagniard*, 1953], where the horizontal electric field is related to the perpendicular horizontal magnetic field by the surface impedance ($Z$, discussed in section 2.2):

$$\tilde{E}_{x,y} = \pm \frac{1}{\mu_0} \tilde{Z} \tilde{B}_{y,x}, \qquad (3)$$
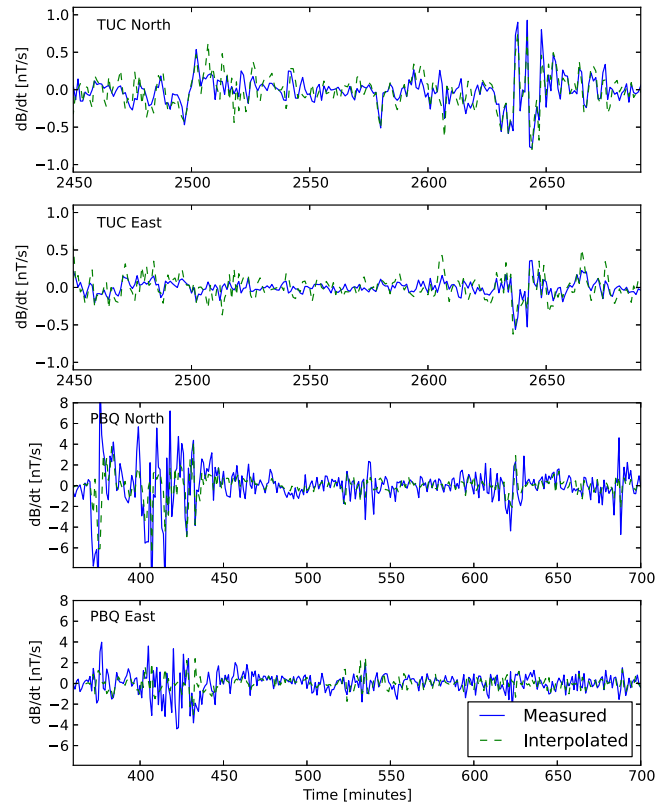


**Figure 4.** Comparison of the measured (solid blue lines) and interpolated (dashed green lines) magnetic field time derivatives for the 2003 "Halloween" storm for the station with the lowest (TUC) and highest (PBQ) RMS deviation. Missing magnetic field data are set to zero and not included in the RMSD calculation. Note that the magnetic field data are separated by 1 min intervals but divided by 60 s to determine $dB/dt$.

where ˜ represents Fourier transformed values in the spectra domain and $\mu_0$ is a constant reflecting the permittivity of free space [e.g., *Viljanen et al.*, 2004]. In Fourier space, the magnetic field is mathematically equivalent to its time derivative divided by its angular frequency $\omega$, so the relationship becomes

$$\tilde{E}_{x,y} = \pm \frac{\tilde{Z}}{\mu_0} \left( \frac{1}{i\,\omega} \frac{\mathrm{d}\tilde{B}_{y,x}}{\mathrm{d}t}(\omega) \right). \qquad (4)$$

[26] For the electric field calculation, we divide the data from the entire storm ($\sim$ 3 days) into 4 h intervals. To deal with edge effects of Fourier transforming a finite time series, we follow the example of *Viljanen et al.* [2006] and extend the beginning and end of each 4 h interval by 4 h on each end with constant values that match the beginning and end values of the data. We multiply the extended data by the Parzen window:

$$W = 1 - \left[ \frac{2(n - N/2)}{N} \right]^8 \qquad (5)$$

for $n$ = 1 to $N$, $N$ = 720 1 min time steps, to force the beginning and end values to be the same. We verified that longer and shorter intervals (ranging from 1 h to the entire storm) do not affect the output electric field. Electric fields at grid locations that fall into oceans, lakes, or Mexico, where we do not have surface impedance models, are set to zero.

### 4.2. Electric Field Maps

[27] Figures 5 and 6 show snapshots of the surface electric field amplitude ($|E| = \sqrt{E_x^2 + E_y^2}$) and direction during the 1989 and 2003 storms, respectively. The electric field amplitudes at the 9100 grid locations are shown as filled contours, with darker colors representing more intense amplitudes. The direction of the electric field, obtained from the vector addition of $E_x$ and $E_y$, are represented by barbs.

[28] The maximum amplitude from our electric field maps is 2.6 V km$^{-1}$ for the 1989 "Quebec" storm and 1.9 V km$^{-1}$ (3.7 V km$^{-1}$ from the Intermagnet data product, see section 4.4) for the 2003 "Halloween" storms. For both storms, the largest electric field amplitudes are found in the Manitoba physiographic region at high latitudes (> 55°). In the Quebec region, the maximum electric field amplitude is 1.4 V km$^{-1}$ for the 1989 storm. It is apparent from Figures 5 and 6 that many regions in Canada experience the strongest electric field fluctuations during the storms.

[29] Strong electric field fluctuations also appear to occur along the Atlantic Coast from Maine to Virginia at times. While it is not surprising that the northeastern region experiences strong electric field amplitudes given its higher magnetic latitude (45°–50°), the large values of $|E|$ along the coast further south and the Gulf of Mexico are unexpected. Maximum electric field amplitudes in the

south reach 0.4 and 0.2 V km$^{-1}$ (0.6 V km$^{-1}$ from the Intermagnet data product) on the panels shown in Figures 5 and 6, respectively. Corresponding maps of the magnetic field time derivative ($|\mathrm{d}B/\mathrm{d}t| = \sqrt{\mathrm{d}B_x^2/\mathrm{d}t + \mathrm{d}B_y^2/\mathrm{d}t}$) show local enhancements in the south around those time periods. Additionally, careful examination of the electric field maps show that the distribution of high/low electric field amplitudes are well-matched to the physiographic regions outlined in Figure 2. This suggests that the response of the physiographic region also contributes to these large electric field amplitudes in the south. We consider the response of the different surface impedance models in section 4.3.

### 4.3. Response of Physiographic Regions

[30] Considering the horizontal electric field maps, it is clear that the surface impedance of different physiographic regions plays a large role in determining the amplitude of the local horizontal electric field.

[31] To facilitate a direct comparison of responses of different physiographic regions, we calculate electric field (equation (4)) using the surface impedances from the 25 different conductivity models with the same set of magnetic field time series (in the North-South and East-West directions). We normalize the peak electric field amplitude ($|E_{\mathrm{peak}}| = \max(\sqrt{E_x^2 + E_y^2})$) from each region to the peak electric field amplitude from the IP1 region. The Interior Plains, IP1, encompasses much of the midwestern and parts of southeastern United States, and its value of $|E_{\mathrm{peak}}|$ is typically near the middle of the distribution of the models, so it is a reasonable choice for normalization. We then rank the conductivity models by the normalized peak electric field value. We repeat this calculation for different magnetic field inputs—using all the measured magnetic fields ($B_x$ and $B_y$) for both storms at all the magnetometer stations listed in Table 1. Thus, for a given magnetometer station, we obtain a set of 25 electric field time series for each direction.

[32] Table 3 shows the ranked list of different surface impedance models, averaged over all the different sets of magnetic field input data. The models are ordered by decreasing intensity. The normalized, averaged $|E_{\mathrm{peak}}|$ ranges over a factor of $\sim$ 35 from 2.41 (MAN) to 0.07 (NOV). We find that relative order of the models do not change much with different input magnetic fields and storms, though a few regions with similar responses ($\Delta |E_{\mathrm{peak}}| \leq$ 0.01, e.g., AK1A and PB1) may switch positions on the ranked list.

[33] The value of the normalized $|E_{\mathrm{peak}}|$, however, *does* change with different input magnetic fields for the same physiographic region. The difference between the lowest and highest value of normalized $|E_{\mathrm{peak}}|$ for all input magnetic fields, averaged over all surface impedance models, is about a factor of 2. The change in relative $|E_{\mathrm{peak}}|$ with different magnetic field inputs highlights how the temporal behavior of the magnetic field affects the response of the physiographic region. $|E_{\mathrm{peak}}|$ cannot be simply
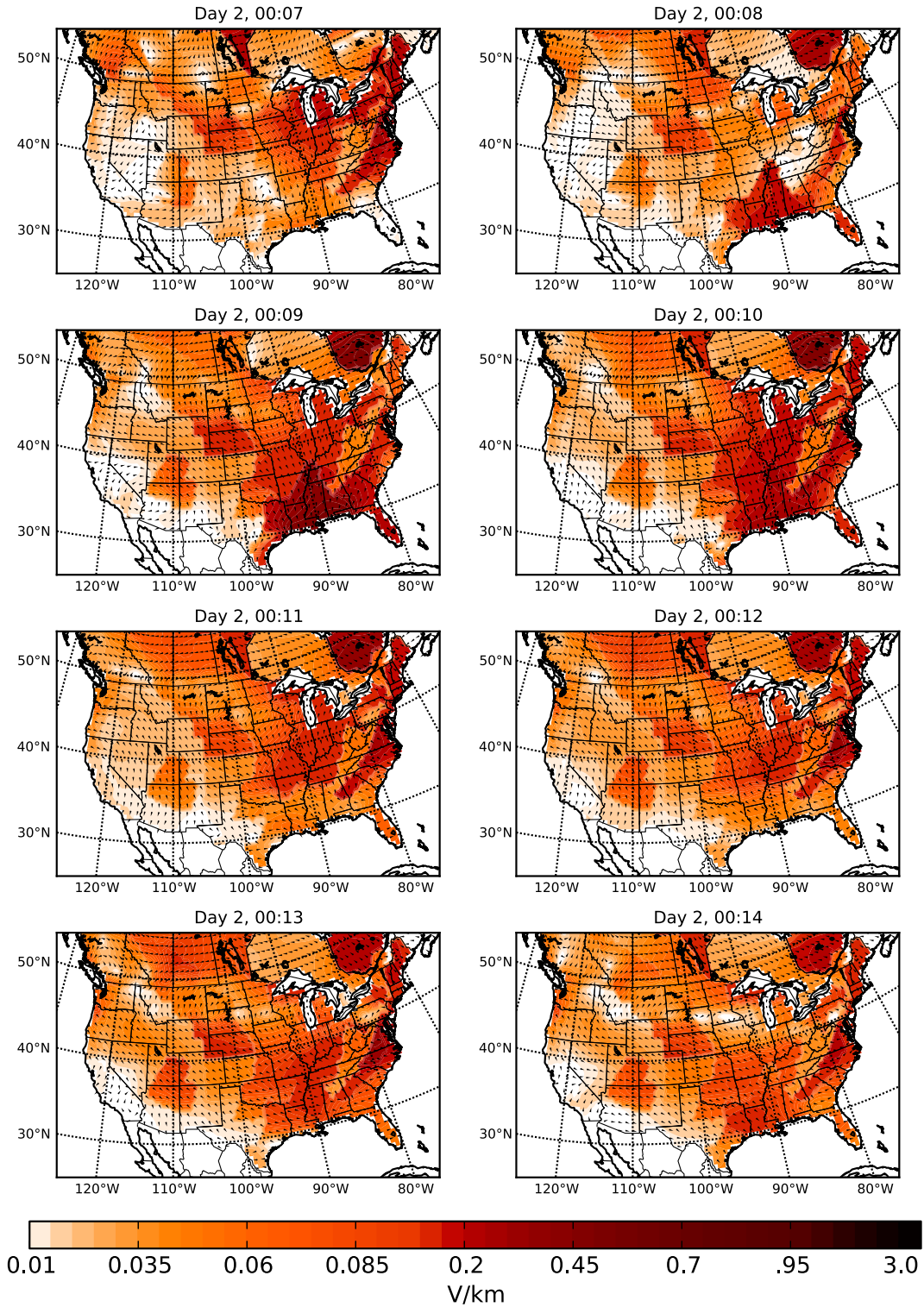
**Figure 5.** Maps of the electric field amplitude (|*E*|, heat scale) and direction (barbs) for eight 1 min time steps during the 1989 "Quebec" storm. Darker colors represent larger values of |*E*|, on a normalized log scale.
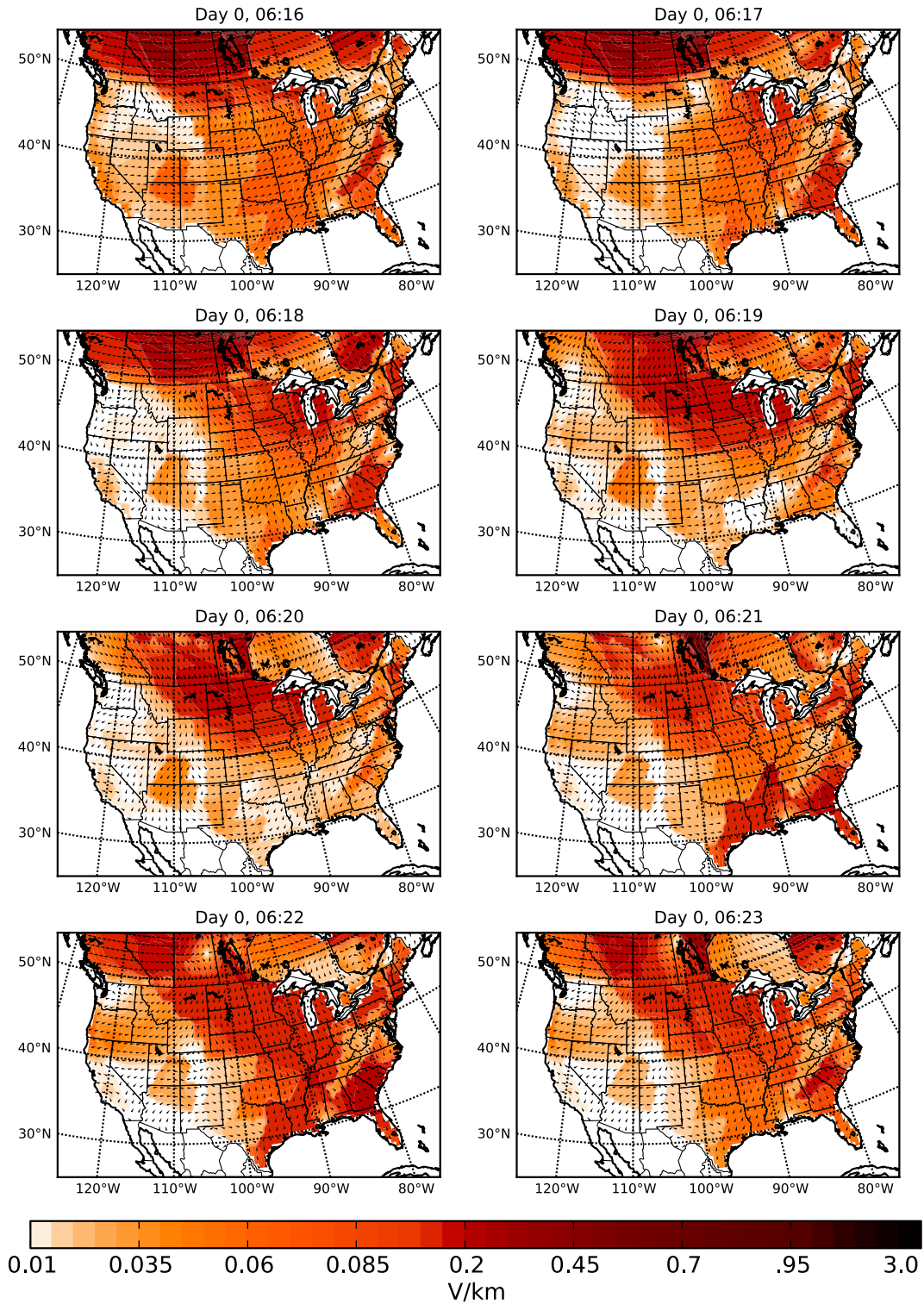
**Figure 6.** Maps of the electric field amplitude (|*E*|, heat scale) and direction (barbs) for eight 1 min time steps during the 2003 "Halloween" storm. Darker colors represent larger values of |*E*|, on a normalized log scale.

WEI ET AL.: HISTORICAL GEOMAGNETIC STORMS

**Table 3.** Relative Peak Electric Field Amplitudes for Different Surface Impedance Models[a]

| Region | Relative $|E_{peak}|$ |
| --- | --- |
| MAN | 2.41 |
| QUE | 2.21 |
| PT1 | 1.92 |
| CP2 | 1.77 |
| CP1 | 1.55 |
| IP3 | 1.33 |
| CL1 | 1.31 |
| SU1 | 1.27 |
| AP2 | 1.20 |
| NE1 | 1.15 |
| IP2 | 1.09 |
| IP1 | 1.00 |
| BRC | 0.84 |
| AK1A | 0.61 |
| PB1 | 0.61 |
| AK1B | 0.59 |
| SL1 | 0.58 |
| PB2 | 0.47 |
| AP1 | 0.42 |
| CS1 | 0.42 |
| BR1 | 0.40 |
| IP4 | 0.40 |
| ONT | 0.39 |
| CO1 | 0.38 |
| NOV | 0.07 |

[a]Normalized to $|E_{peak}|$ for IP1 and averaged over different input magnetic field time series from the 1989 and 2003 storms recorded at magnetometer stations listed in Table 1.

scaled between different surface impedance models with a linear function.

[34] Figure 7 shows again the different physiographic regions included in our study, this time color-coded by the value of $|E_{peak}|$ relative to IP1 averaged over different magnetic field inputs. Note that this figure only shows the risk of spatially uniform, intense horizontal electric fields based on the response of the physiographic region. It does not take into account the fact that regions at higher magnetic latitudes tend to experience stronger magnetic fields. In Canada, the Quebec and Manitoba provinces appear to have the strongest response, while Nova Scotia and Ontario have relatively weak responses. In the United States, Figure 7 emphasizes the fact that regions along the Atlantic Coast and especially along the Gulf of Mexico may experience enhanced surface electric field fluctuations during a geomagnetic storm despite its lower magnetic latitude.

### 4.4. Comparison of Intermagnet and SuperMAG Data

[35] For comparison, we examine the electric field maps derived from the Intermagnet Definitive and the Super-MAG Final data products for the same magnetometer stations over the same time range for the 2003 storm. The electric fields, derived from interpolated magnetic fields (section 3.1) combined with the regional resistivity models (section 2.2), appear to be almost identical despite any constant offsets in the input magnetic field (Figure 8, left

column). The mean difference is around zero for all locations and time steps (2.0 and $-0.2 \times 10^{-4}$ V km$^{-1}$ for the East and North components, respectively), with standard deviations of 0.03 and 0.02 V km$^{-1}$. However, the maximum electric field amplitude ($|E| = \sqrt{E_x^2 + E_y^2}$) derived from the two data sets differs by almost a factor of 2.

[36] Figure 8 illustrates the different uncertainties that contribute to errors in the electric field estimate. While linear baseline offsets in the magnetic field data do not affect the electric field estimate (Figure 8, left column), linear interpolation of missing data greatly reduces the electric field amplitudes as the magnetic field variation is smoothed (Figure 8, middle column).

[37] This is analogous to the reduction in electric field amplitudes derived from lower cadence magnetic field measurements. For example, *Radasky et al.* [1993] showed that 2 s magnetic field data resulted in higher estimated electric field amplitudes than 1 min data. More recently, *Pulkkinen et al.* [2006] found that while the maximum d$B$/d$t$ values are significantly lower in data with longer time steps, the maximum surface electric field decreases by only 20%. Thus, while we would expect higher amplitudes still in section 4.2 if 1 s data were available for the historical storms, it is unclear how important these differences are for calculating practical effects on power systems. This
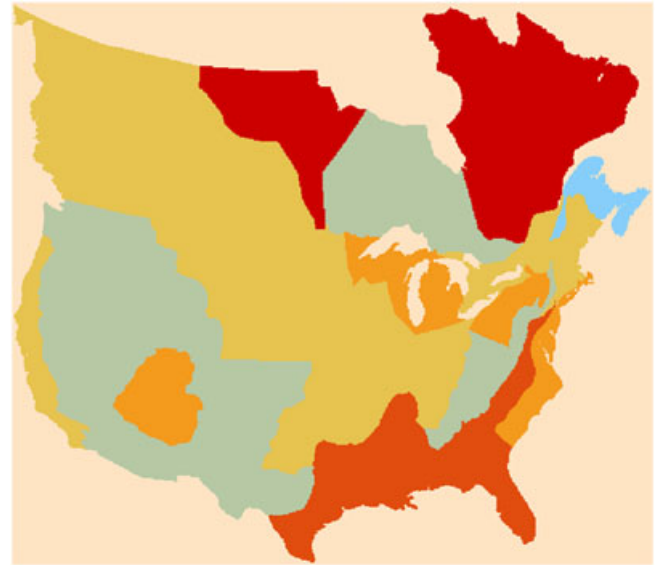


**Figure 7.** Physiographic regions in the United States and Canada, color-coded by maximum electric field amplitude averaged over different input magnetic field time series. Note that this only reflects ground conductivity risk (i.e., essentially assuming spatially uniform magnetic field variations) and does not account for the fact that regions at higher magnetic latitudes tend to experience stronger magnetic field fluctuations. The colors are in the order of red, dark orange, orange, yellow, green, and blue for regions with the highest to lowest values of $|E_{peak}|$.
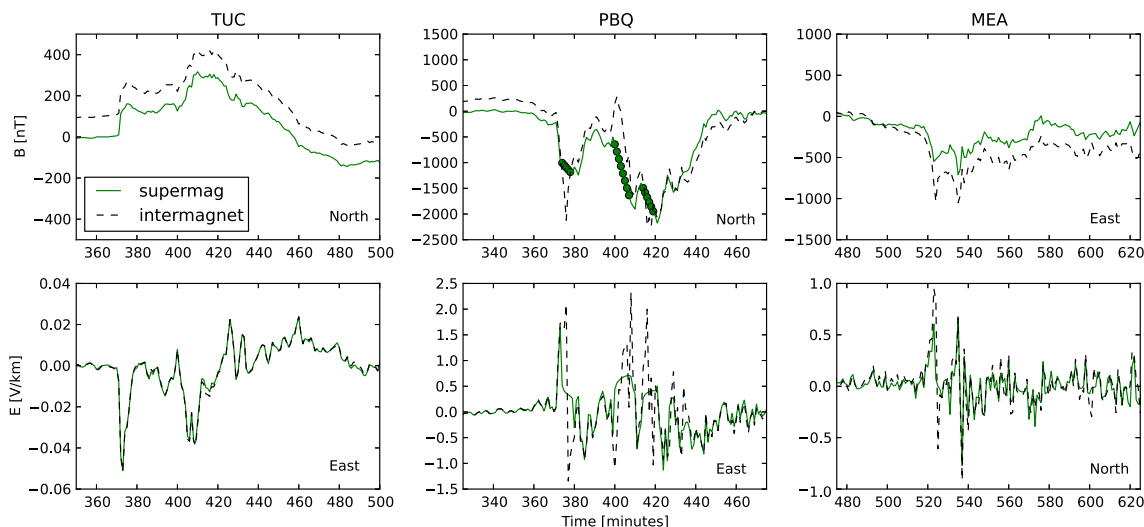
**Figure 8.** (top row) Comparison of magnetic fields from different magnetometer stations for the 2003 storm from SuperMAG Final (solid green line) and Intermagnet Definitive (dashed black line) data products. (bottom row) The corresponding electric fields derived for the perpendicular direction are also shown. Overall, the two electric field time series are very similar despite any constant offsets (TUC) in the input magnetic field, although the data derived from Intermagnet tend to have larger electric field amplitudes at times. This is most often due to missing data in the SuperMAG Final data product that we linearly interpolate (filled green circles, PBQ). Nonlinear differences in the baseline of the magnetic field (MEA) can also contribute to differences in the electric field.

is an area that would benefit from more research, especially since measured power system effects are correlated with estimated electric fields. Fortunately, magnetometer data from the past few years are available in 1 s time steps and can be used to better validate GIC calculations against measured data.

[38] Another source of uncertainty in the electric field estimates are nonlinear baseline errors, which result in noticeable differences in the output electric field (Figure 8, right column). Considering that these sources of error can affect different magnetometer stations at different times, this introduces an additional source of error during the magnetic field interpolation, as the interpolated magnetic fields will have some combination of these data issues. One way to validate the electric field estimates would be against GIC recordings through power flow modeling.

### 4.5. The Coast Effect

[39] We mention here the fact that the coast effect is not included in our estimates of the surface electric fields. The coast effect, which enhances the electric field amplitudes near the ocean, reflects the excellent conductivity of salt water.

[40] The coast effect can and has been included in the conductivity profiles used to estimate the electric field [e.g., *Lambert and Caner*, 1965; *Schmucker*, 1965; *Banerjee et al.*, 1998] but is often restricted to small regions where detailed geomagnetic soundings are available. More general models have been developed in the

recent years [e.g., *Olsen and Kuvshinov*, 2004; *Gilbert*, 2005] but still require knowledge of regional bathymetry and topography that is outside the scope of this paper. Thus, we defer the inclusion of the coast enhancement for a more detailed study of smaller regions and note that the electric field amplitudes along the coasts are likely to be much higher when this boundary is included in surface impedance models.

## 5. Discussion

[41] As described in section 1, the best way to understand the risk to the electric grid during geomagnetic disturbances is to accurately model the flow of geomagnetically induced currents in transmission lines during these storms. GICs can be estimated by integrating the electric field along the transmission lines, but a realistic representation of the horizontal electric field during the disturbance is essential. From the results of sections 4.2 and 4.3, it is clear that the response of the surface impedance model for different physiographic regions plays a key role in determining the surface electric field strength, as we observe large electric field fluctuations in regions with high resistivities. While the boundaries of the physiographic regions are quite large, power system regions are highly interconnected and cover large areas. With long AC transmission lines of approximately few hundred kilometers in length, a good estimate of the spa-

tial variations of the surface electric field is very important for GIC modeling.

[42] The surface electric field maps we present in this paper are the most realistic representation to date of the spatial and temporal surface electric field variations during two major historical geomagnetic storms in North America. The maps are suitable for identifying regions, grid assets, and populations at risk from power outages resulting from large electric field fluctuations and allow appropriate preparations to be made.

[43] Additionally, the maps can be used to estimate the GIC flowing along transmission lines in 1 min intervals during the storms. Although it is likely that the 1 min time steps of the historical data smooths out magnetic field variations on shorter timescales and artificially lowers the electric field amplitude estimates, they are still useful for setting the lower limit on GICs during these time periods. High levels of GIC flow can not only heat and damage transformers but also increase the consumption of reactive power [e.g., *Dong et al.*, 2001; *Berge et al.*, 2011], leading to system instabilities and cascading voltage collapse [*Albertson et al.*, 1981; *Schlueter*, 1998]. Used as inputs to power flow software to model grid behavior during the storm, the horizontal electric field time series will allow grid owners to identify vulnerable transformers that can be protected and formulate procedures for grid operations during disturbances to avoid large-scale outages.

[44] Finally, the historical storm scenarios are not only useful for examining the grid response to a typical storm, they can be scaled up to simulate stronger geomagnetic disturbances such as the 100 year, Carrington-level storm. While a Carrington-level storm is unlikely to occur in a given year [*Love*, 2012], these events are far from impossible and can have devastating consequences if we are not properly prepared.

## 6. Summary

[45] In this paper, we consider magnetometer data from two historical geomagnetic disturbances—the 1989 "Quebec" storm and the 2003 "Halloween" storms. We interpolate the sparsely distributed magnetometer data across much of North America using the Spherical Elementary Current System and combine them with local models of surface impedances using the plane wave method to estimate the horizontal, orthogonal electric fields. We summarize our results below.

[46] 1. In general, the SECS method does a good job recovering the overall trend of the horizontal magnetic field variations. Larger RMS deviations are observed at higher latitudes, which appears to reflect the stronger magnetic field fluctuations at those locations.

[47] 2. From our electric field maps, we find the maximum electric field amplitudes for the 1989 and 2003 storms to be 2.6 and 1.9 V km$^{-1}$ (3.7 V km$^{-1}$ from the Intermagnet data product), respectively, occurring in the Manitoba region of Canada. Large horizontal electric field variations

are also observed in the Quebec region, where the maximum electric field amplitude reached 1.4 V km$^{-1}$ for the 1989 storm. These amplitudes are likely lower limits due to the smoothing of more rapid fluctuations in the historical 1 min magnetic field data.

[48] 3. In addition to large electric field variations observed in Canada during both storms, large variations are also seen along the Atlantic and Gulf Coast further south. This is primarily due to the high resistivity of these physiographic regions. Because the USGS models are still very data limited, these results should be confirmed through an expanded field program.

[49] 4. Comparing the responses of different surface impedance models to the same input magnetic field time series, we find that the peak electric field amplitude ranges over a factor of $\sim 35$ from the least (NOV) to most (MAN) responsive physiographic region. Normalized to the peak electric field amplitude of the Interior Plains, the relative peak electric field from each region changes with different input magnetic fields, varying by a factor of 2. The relative ranking of the responses, however, do not change by much.

[50] 5. Comparison of the electric fields derived for the 2003 storm from the SuperMAG Final and the Intermagnet Definitive data products yield very similar results, although the maximum electric field amplitudes derived from the two data sets differs by almost a factor of two. Uncertainties from the interpolation of missing magnetic field data and nonlinear baseline differences between the SuperMAG and Intermagnet data products contribute to these differences.

## References

Albertson, V., J. Kappenman, N. Mohan, and G. A. Skarbakka (1981), Load-flow studies in the presence of geomagnetically-induced currents, *IEEE Trans. Power Apparatus Syst.*, *PAS-100* (2), 594–607, doi:10.1109/TPAS.1981.316916.

Amm, O. (1997), Ionospheric elementary current systems in spherical coordinates and their application, *J. Geomagn. Geoelectr.*, *49*, 947–955.

Amm, O., and A. Viljanen (1999), Ionospheric disturbance magnetic field continuation from the ground to the ionosphere using

spherical elementary current systems, *Earth Planet Space*, *51*, 431–440.

Banerjee, B., P. B. V. S. Rao, G. Gupta, E. J. Joseph, and B. P. Singh (1998), Results from a magnetic survey and geomagnetic depth sounding in the post-eruption phase of the Barren Island volcano, *Earth Planet Space*, *50*, 327–338.

Berge, J., R. Varma, and L. Marti (2011), Laboratory validation of the relationship between Geomagnetically Induced Current (GIC) and transformer absorbed reactive power, in *2011 IEEE Electrical Power and Energy Conference (EPEC)*, pp. 491–495, IEEE, Winnipeg, Manit, doi:10.1109/EPEC.2011.6070251.

Bolduc, L. (2002), GIC observations and studies in the Hydro-Québec power system, *J. Atmos. Sol. Terr. Phys.*, *64*(16), 1793–1802, doi:10.1016/S1364-6826(02)00128-1.

Boteler, D. (2001), Assessment of geomagnetic hazard to power systems in Canada, *Nat. Hazard.*, *23*(2-3), 101–120, doi:10.1023/A:1011194414259.

Boteler, D. H., R. J. Pirjola, and H. Nevanlinna (1998), The effects of geomagnetic disturbances on electrical systems at the Earth's surface, *Adv. Space Res.*, *22*, 17–27, doi:10.1016/S0273-1177(97)01096-X.

Cagniard, L. (1953), Basic theory of the magneto-telluric method of geophysical prospecting, *Geophysics*, *18*(3), 605–635.

Carr, S. D., R. M. Easton, R. A. Jamieson, and N. G. Culshaw (2000), Geologic transect across the Grenville orogen of Ontario and New York, *Can. J. Earth Sci.*, *37*(2-3), 193–216, doi:10.1139/e99-074.

Dong, X., Y. Liu, and J. Kappenman (2001), Comparative analysis of exciting current harmonics and reactive power consumption from GIC saturated transformers, in *Power Engineering Society Winter Meeting, 2001,* vol. 1, pp. 318–322, IEEE, Columbus, Ohio, doi:10.1109/PESW.2001.917055.

Erinmez, I. A., S. Majithia, C. Rogers, T. Yasuhiro, S. Ogawa, H. Swahn, and J. G. Kappenman (2002), Application of modeling techniques to assess geomagnetically induced current risks on the NGC transmission system, in *CIGRE Session*, pp. 39–304, CIGRE, Paris, France.

Fernberg, P. (2012), One-dimensional Earth resistivity models for selected areas of continental United States and Alaska, *EPRI Technical Update, 1026430*.

Forbes, K. F., and O. C. St. Cyr (2012), Did geomagnetic activity challenge electric power reliability during solar cycle 23?, Evidence from the PJM regional transmission organization in North America, *Space Weather*, *10*, S05001, doi:10.1029/2011SW000752.

Gaunt, C., and G. Coetzee (2007), Transformer failures in regions incorrectly considered to have low GIC-risk, in *Power Tech, 2007 IEEE Lausanne*, pp. 807–812, IEEE, Lausanne, France, doi:10.1109/PCT.2007.4538419.

Gilbert, J. L. (2005), Modeling the effect of the ocean-land interface on induced electric fields during geomagnetic storms, *Space Weather*, *3*, S04A03, doi:10.1029/2004SW000120.

Gjerloev, J. W. (2012), The SuperMAG data processing technique, *J. Geophys. Res.*, *117*, A09213, doi:10.1029/2012JA017683.

Horton, R., D. Boteler, T. Overbye, R. Pirjola, and R. C. Dugan (2012), A test case for the calculation of geomagnetically induced currents, *IEEE Trans. Power Delivery*, *27*(4), 2368–2373, doi:10.1109/TPWRD.2012.2206407.

Kappenman, J., and V. D. Albertson (1990), Bracing for the geomagnetic storms, *IEEE Spectr.*, *27*(3), 27–33, doi:10.1109/6.48847.

Kappenman, J., V. Albertson, and N. Mohan (1981), Investigation of geomagnetically induced currents in the proposed Winnipeg-Duluth-twin cities 500-kV transmission line, *NASA STI/Recon Technical Report N.* 82, 15345, http://adsabs.harvard.edu/abs/1981STIN...8215345K.

Kappenman, J., W. Radasky, J. Gilbert, and L. Erinmez (2000), Advanced geomagnetic storm forecasting: A risk management tool for electric power system operations, *IEEE Trans. Plasma Sci.*, *28*(6), 2114–2121, doi:10.1109/27.902238.

Kappenman, J. G. (2004), The evolving vulnerability of electric power grids, *Space Weather*, *2*, S01004, doi:10.1029/2003SW000028.

Kappenman, J. G. (2010), Geomagnetic storms and their impacts on the U.S. power grid, *Metatech-R-319*, Oak Ridge, Tenn.

Kappenman, J. G., and W. A. Radasky (2005), Too important to fail, *Space Weather*, *3*, S05001, doi:10.1029/2005SW000152.

Lambert, A., and B. Caner (1965), Geomagnetic depth-sounding and the coast effect in Western Canada, *Can. J. Earth Sci.*, *2*, 485–509, doi:10.1139/e65-039.

Love, J. J. (2012), Credible occurrence probabilities for extreme geophysical events: Earthquakes, volcanic eruptions, magnetic storms, *Geophys. Res. Lett.*, *39*, L10301, doi:10.1029/2012GL051431.

McLay, S. A., and C. D. Beggan (2010), Interpolation of externally-caused magnetic fields over large sparse arrays using spherical elementary current systems, *Ann. Geophys.*, *28*(9), 1795–1805, doi:10.5194/angeo-28-1795-2010.

Molinski, T. S. (2002), Why utilities respect geomagnetically induced currents, *J. Atmos. Sol. Terr. Phys.*, *64*, 1765–1778, doi:10.1016/S1364-6826(02)00126-8.

Olsen, N., and A. Kuvshinov (2004), Modeling the ocean effect of geomagnetic storms, *Earth Planet Space*, *56*, 525–530.

Pirjola, R. (2008), Effects of interactions between stations on the calculation of geomagnetically induced currents in an electric power transmission system, *Earth Planet Space*, *60*, 743–751.

Pirjola, R., D. Boteler, and L. Trichtchenko (2009), Ground effects of space weather investigated by the surface impedance, *Earth Planet Space*, *61*, 249–261.

Press, W. H., S. A. Teukolsky, W. T. Vetterling, and B. P. Flannery (2007), *Numerical Recipes 3rd Edition: The Art of Scientific Computing*, 65–67, Cambridge Univ. Press, New York.

Pulkkinen, A., O. Amm, and A. Viljanen (2003), Ionospheric equivalent current distributions determined with the method of spherical elementary current systems, *J. Geophys. Res.*, *108*(A2), 1053, doi:10.1029/2001JA005085.

Pulkkinen, A., O. Amm, A. Viljanen, and Bear Working Group (2003), Separation of the geomagnetic variation field on the ground into external and internal parts using the spherical elementary current system method, *Earth Planet Space*, *55*, 117–129.

Pulkkinen, A., S. Lindahl, A. Viljanen, and R. Pirjola (2005), Geomagnetic storm of 29–31 October 2003: Geomagnetically induced currents and their relation to problems in the Swedish high-voltage power transmission system, *Space Weather*, *3*, S08C03, doi:10.1029/2004SW000123.

Pulkkinen, A., A. Viljanen, and R. Pirjola (2006), Estimation of geomagnetically induced current levels from different input data, *Space Weather*, *4*, S08005, doi:10.1029/2006SW000229.

Pulkkinen, A., E. Bernabeu, J. Eichner, C. Beggan, and A. W. P. Thomson (2012), Generation of 100-year geomagnetically induced current scenarios, *Space Weather*, *10*, S04003, doi:10.1029/2011SW000750.

Radasky, W. A., M. A. Messier, J. Kappenman, S. Norr, and R. Parenteau (1993), Presentation and analysis of geomagnetic storm signals at high data rates, in *1993 IEEE International Symposium on Electromagnetic Compatibility, 1993. Symposium Record*, pp. 156–157, IEEE, Dallas, Tex., doi:10.1109/ISEMC.1993.473760.

Schlueter, R. (1998), A voltage stability security assessment method, *IEEE Trans. Power Syst.*, *13*(4), 1423–1438, doi:10.1109/59.736286.

Schmucker, U. (1965), Anomalies of geomagnetic variations in the southwestern United States, *Bull. Scripps Inst. Oceanogr.*, *13*, 1–165.

Thomson, A. W. P., A. J. McKay, E. Clarke, and S. J. Reay (2005), Surface electric fields and geomagnetically induced currents in the Scottish Power grid during the 30 October 2003 geomagnetic storm, *Space Weather*, *3*, S11002, doi:10.1029/2005SW000156.

Viljanen, A., A. Pulkkinen, O. Amm, R. Pirjola, T. Korja, and B. W. Group (2004), Fast computation of the geoelectric field using the method of elementary current systems and planar Earth models, *Ann. Geophys.*, *22*(1), 101–113, doi:10.5194/angeo-22-101-2004.

Viljanen, A., A. Pulkkinen, R. Pirjola, K. Pajunp, P. Posio, and A. Koistinen (2006), Recordings of geomagnetically induced currents and a nowcasting service of the Finnish natural gas pipeline system, *Space Weather*, *4*, S10004, doi:10.1029/2006SW000234.

Viljanen, A., R. Pirjola, M. Wik, A. Ádám, E. Prácser, Y. Sakharov, and J. Katkalov (2012), Continental scale modelling of geomagnetically induced currents, *J. Space Weather Space Clim.*, *2*(26), A17, 1–11, doi:10.1051/swsc/2012017.

Wik, M., A. Viljanen, R. Pirjola, A. Pulkkinen, P. Wintoft, and H. Lundstedt (2008), Calculation of geomagnetically induced currents in the 400 kV power grid in southern Sweden, *Space Weather*, *6*, S07005, doi:10.1029/2007SW000343.